# The PSE-sponge method for simulating natural transition in WMLES

**By C. A. Gonzalez, S. R. Harris† AND P. Moin**

Accurate prediction of the laminar-to-turbulent transition in boundary layers remains challenging for wall-modeled large-eddy simulations (WMLESs), particularly on coarse computational grids. The thin laminar region preceding transition requires significantly higher grid resolution than turbulent regions, making high-fidelity simulations computationally expensive. This study presents a novel hybrid approach combining nonlinear parabolized stability equations (NLPSE) with WMLES to efficiently simulate transitional flows.

We introduce the PSE-sponge method, which directly couples PSE solutions with LES through sponge-layer forcing. The method is validated on flat-plate cases and successfully applied to transition simulation on an NLF(01)-0416 natural laminar flow airfoil, where conventional WMLES approaches fail. Sensitivity analysis reveals robust performance across key parameters, including sponge strength and number of PSE modes.

## 1. Introduction

Accurate prediction of the laminar-to-turbulent transition in boundary layers remains one of the most challenging problems in computational fluid dynamics, with profound implications for the design and analysis of aerospace vehicles. The location and extent of transition directly influence skin friction, heat transfer and ultimately vehicle performance through their impact on drag and thermal loads. Despite decades of research, the simulation of transitional flows at practical Reynolds numbers continues to present fundamental computational challenges, particularly for wall-modeled large-eddy simulations (WMLESs) that have become the standard for industrial applications.

The computational difficulty stems from the disparate length scales characterizing laminar and turbulent boundary layers. In the pre-transitional regime, accurate resolution of instability growth requires 10–100 times more grid points than in fully turbulent regions to capture the amplification of disturbances preceding breakdown (Slotnick *et al.* 2014). This resolution requirement poses a significant barrier to the application of high-fidelity simulation methods to realistic engineering configurations, where computational resources must be allocated efficiently across complex geometries.

Current approaches to transition modeling in LES face fundamental limitations. Traditional equilibrium wall models, designed for fully turbulent flows, assume a constant stress layer that does not exist in laminar or transitional boundary layers. When applied to transitional flows, these models overestimate momentum drain at the wall, triggering premature transition regardless of the actual instability mechanisms present in the flow. Conversely, wall-resolved LES (WRLES) with no-slip boundary conditions can capture transition physics accurately but requires grid resolutions approaching those of direct numerical simulation (DNS), with computational costs scaling as for WRLES $Re^{1.86}$

† Sandia National Laboratories

compared to $Re^{2.64}$ for DNS (Choi & Moin 2012), making it intractable for practical Reynolds numbers of interest.

Natural transition in low-disturbance environments typically proceeds through the growth of exponential instabilities. In zero-pressure-gradient boundary layers, the Tollmien-Schlichting (TS) wave represents the primary viscous instability becoming active above a critical Reynolds number. The subsequent path to turbulence depends on the secondary instability mechanisms. In K-type transition (Kachanov *et al.* 1977), three-dimensionality is provided by oblique modes at the same frequency as the TS wave. This fundamental frequency interaction causes the growth of higher harmonics and weakly nonlinear dynamics, leading to the development of streamwise-aligned Λ-shaped vortices. These vortices have two elongated legs of oppositely signed streamwise vorticity and a tip of spanwise vorticity characteristic of hairpin vortices. The key feature of K-type transition is that the oblique modes oscillate at the fundamental TS frequency, creating a coherent resonance that produces Λ-vortices arranged in a regular, streamwise-aligned grid pattern.

An alternative path to transition begins with excitation of a TS wave supplemented by subharmonic oblique modes, known as H-type transition (Herbert 1988). In contrast to K-type transition, the oblique modes in H-type transition oscillate at exactly half the frequency of the fundamental TS wave. This subharmonic frequency relationship creates a different nonlinear interaction mechanism that similarly leads to the formation of Λ-vortices, though, in contrast to the streamwise-aligned grid formation of K-type transition, in H-type transition the vortices develop in a staggered formation. The subharmonic nature of the oblique disturbances fundamentally alters the phase relationships and growth rates, resulting in this characteristic staggered vortex arrangement.

Oblique transition represents a fundamentally different transition scenario that is initiated by two oblique modes with opposite wave angles without the presence of a TS mode (Klebanoff *et al.* 1962). In this pathway, the transition process bypasses the traditional TS wave mechanism entirely. The two oblique waves, typically inclined at equal but opposite angles to the streamwise direction, interact nonlinearly to generate counter-rotating streamwise vortices. These vortices are the primary mechanism for energy transfer from the oblique waves to the mean flow. The dominant feature of oblique transition is the emergence of large-amplitude, spanwise-periodic streamwise streaks that grow inside the boundary layer. As these oblique waves propagate downstream, their nonlinear interaction generates and strengthens counter-rotating streamwise vortices, which in turn amplify the streamwise streaks through a lift-up mechanism. For large initial amplitudes, the periodic streaks grow in amplitude and become increasingly unstable, eventually leading to secondary instabilities and breakdown to turbulence (Berlin *et al.* 1999).

The parabolized stability equations offer an efficient framework for analyzing disturbance evolution in spatially developing flows that captures nonparallel effects crucial for accurate growth rate prediction. Recent work by Lozano-Durán *et al.* (2018) and Gonzalez *et al.* (2023) demonstrated that the nonlinear form (NLPSE) could generate accurate inflow conditions for DNS of transitional boundary layers, suggesting the potential for hybrid PSE-LES methodologies.

Building on this foundation, the present study develops a unified framework combining NLPSE with WMLES to enable efficient and accurate simulation of transitional flows at practical Reynolds numbers. The PSE-sponge technique directly couples PSE solutions with LES through volumetric forcing, eliminating geometric constraints associated with complex inlet specifications. This method leverages the Falkner-Skan wall model (FSWM)

to generate accurate laminar base flows from coarse LES grids (Gonzalez *et al.* 2021). The framework is validated through systematic studies of canonical transition scenarios and demonstrated on the NLF(01)-0416 natural laminar flow airfoil. We show that the hybrid NLPSE–WMLES approach accurately predicts transition location, skin friction evolution and characteristic flow structures while reducing computational requirements compared to traditional high-fidelity methods.

## 2. Mathematical background

The incompressible PSE formulation, introduced by Herbert (1997) and Bertolotti *et al.* (1992), decomposes the flow field state vector $\overline{\boldsymbol{\phi}}(x, y)$ into a steady base state $\boldsymbol{\Phi}(x, y) = (U, V, W, P)^T$ and an unsteady perturbation $\boldsymbol{\phi}(x, y, z, t) = (u, v, w, p)^T$ in a body-fitted coordinate system with streamwise ($x$), wall-normal ($y$) and spanwise ($z$) directions, with $u$, $v$ and $w$ being their respective directions and $p$ the pressure. The introduction of this decomposition into the Navier-Stokes equations and subtraction of the mean-flow terms yields

$$\nabla \cdot \boldsymbol{u} = 0, \tag{2.1}$$

$$\frac{\partial \boldsymbol{u}}{\partial t} + \boldsymbol{U} \cdot \nabla \boldsymbol{u} + \boldsymbol{u} \cdot \nabla \boldsymbol{U} + \frac{1}{\rho} \nabla p - \frac{1}{Re} \triangle \boldsymbol{u} = -\boldsymbol{u} \cdot \nabla \boldsymbol{u}, \tag{2.2}$$

where $\rho$ is the fluid density, and $Re$ is the Reynolds number. The perturbation field is represented through a wave-like ansatz,

$$\boldsymbol{\phi}(t, x, y, z) = \sum_{m=-M}^{M} \sum_{n=-N}^{N} \hat{\boldsymbol{\phi}}_{mn}(x, y) \exp\left( i \int_0^x \alpha_{mn}(x') dx' + in\beta z - im\omega t \right), \tag{2.3}$$

where $\hat{\boldsymbol{\phi}}_{mn}$ are slowly varying shape functions, $\alpha_{mn}$ is the complex streamwise wave number, $\beta$ is the real spanwise wave number and $\omega$ is the real temporal frequency. This separation of fast and slow streamwise variations enables coarse streamwise grids while capturing rapid oscillations and exponential growth through the exponential term.

Substituting this ansatz into Eqs. 2.1 and 2.2, assuming a slowly varying baseflow and retaining terms up to $O(Re^{-1})$ yields a parabolic system efficiently solved through spatial marching

$$\sum_{m=-M}^{M} \sum_{n=-N}^{N} \left( \left[ \mathcal{A}\hat{\boldsymbol{\phi}} + \mathcal{B}\frac{\partial \hat{\boldsymbol{\phi}}}{\partial y} + \mathcal{C}\frac{\partial^2 \hat{\boldsymbol{\phi}}}{\partial y^2} + \mathcal{D}\frac{\partial \hat{\boldsymbol{\phi}}}{\partial x} + \mathcal{E}\frac{\partial^2 \hat{\boldsymbol{\phi}}}{\partial x \partial y} \right]_{(m,n)} \right) = \mathcal{NL}_{(m,n)}, \tag{2.4}$$

where each $(m, n)$ mode corresponds to a system of equations. The forcing term $\mathcal{NL}_{(m,n)}$ accounts for the nonlinear terms on the right-hand side of Eq. 2.2. The entries for the incompressible PSE operators can be found in Gonzalez *et al.* (2024).

Standard boundary conditions are imposed on the disturbance quantities for the solution of the NLPSE. The velocity disturbances obey the no-slip condition at the wall

$$\Big( u, v, w \Big) \Big|_{y=0} = 0. \tag{2.5}$$

In the freestream, the $u$ and $w$ velocity perturbations decay to zero while a Neumann boundary condition is set for the $v$ vertical velocity which allows for the development of mean flow distortion

$$\left(u, \frac{\partial v}{\partial y}, w\right)\Big|_{y\to\infty} = 0. \tag{2.6}$$

There is an ambiguity in the solution to this system due to the streamwise variation of both $\hat{\phi}$ and $\alpha_{(m,n)}$. This is resolved via the constraint

$$\int_\Omega \hat{\boldsymbol{\phi}}^H \frac{\partial \hat{\boldsymbol{\phi}}}{\partial x} dy = 0. \tag{2.7}$$

For this study, we use the open-source parallel NLPSE solver glimPSE, which has been extensively verified against canonical transition scenarios Gonzalez *et al.* (2023, 2024). The solver implements implicit Euler marching with stabilization techniques for residual ellipticity and MPI parallelization for efficient multi-mode computation.

## 3. PSE-sponge simulations

While the NLPSE–WMLES methodology demonstrated in Lozano-Durán *et al.* (2018) and Gonzalez *et al.* (2021) successfully enables the efficient simulation of transitional boundary layers on flat plates, the approach faces significant limitations when applied to complex geometries. The primary challenge lies in generating spatially and temporally varying inflow conditions that must be specified at every point along the inlet boundary of the LES domain. For complex configurations such as airfoils, wings or other curved surfaces, the implementation of PSE-generated inflows becomes increasingly cumbersome and computationally expensive. The need to interpolate PSE solutions onto arbitrary inlet geometries, combined with the requirement to maintain phase coherence of disturbances across the entire inlet plane, poses substantial practical difficulties. To address these limitations, we introduce the PSE-sponge method, which represents a paradigm shift from using PSE as a boundary condition generator to employing it as a volumetric forcing mechanism within the LES domain itself. Rather than restricting the PSE solution to providing inflow data, the sponge approach integrates the NLPSE directly into the governing equations through source terms that drive the LES solution toward the PSE-predicted state in specified regions of the computational domain.

The methodology begins with a precursor simulation employing the Falkner-Skan wall model (Gonzalez *et al.* 2020, 2021) to generate accurate laminar base states to be used in the PSE simulation. The NLPSE is then initialized using these baseflow profiles and marched downstream to compute the spatial evolution of instability modes and mean flow distortion. However, rather than terminating the PSE march at the transition point and using the final station as an inflow condition, the sponge approach utilizes the complete PSE solution throughout the transitional region to provide continuous volumetric forcing within the LES domain.

We introduce the PSE-sponge method, which augments the filtered Navier-Stokes equations with volumetric forcing terms,

$$\frac{\partial \overline{\rho}}{\partial t} + \frac{\partial \overline{\rho}\tilde{u}_j}{\partial x_j} = \sigma^*(\overline{\rho}_{PSE} - \overline{\rho}), \tag{3.1}$$

$$\frac{\partial \overline{\rho}\tilde{u}_i}{\partial t} + \frac{\partial}{\partial x_j}[\overline{\rho}\tilde{u}_i\tilde{u}_j + \overline{p}\delta_{ij} - \tilde{\tau}_{ij} + \tau_{ij}^{sgs}] = \sigma^*[(\overline{\rho}\tilde{u}_i)_{PSE} - \overline{\rho}\tilde{u}_i], \tag{3.2}$$

where $\sigma^* = \omega_F\sigma/(2\pi)$ is the dimensional sponge strength, $\sigma$ is its nondimensional counterpart and $\omega_F$ is the temporal frequency associated with the primary disturbance in the flow. The method transitions from PSE-guided physics to standard WMLES through

$$\gamma = 0.5\left(1 + \tanh\left(\frac{(x - x_{tr})\alpha_0}{2\pi}\right)\right), \tag{3.3}$$

applied to both volumetric forcing ($\sigma_{eff} = (1-\gamma)\sigma$) and wall stress ($\tau_w = (1-\gamma)\tau_{PSE} + \gamma\tau_{EQWM}$).

This approach offers several distinct advantages over the inlet-based methodology. First, it eliminates the geometric constraints associated with specifying complex inlet conditions, making the method readily applicable to arbitrary geometries. Second, it provides greater flexibility in domain decomposition, allowing the PSE and LES regions to overlap seamlessly without requiring precise matching at discrete interface locations.

### 3.1. *Flat-plate simulations*

To validate the PSE-sponge methodology and assess its mesh sensitivity, we apply the approach to three canonical transition scenarios, H-type, K-type and oblique transitions. We present results using the five most energetic modes from each transition scenario interpolated from the NLPSE solution onto the LES domain. For H-type transition, this corresponds to the modes $(2,0)$, $(1,1)$, $(3,1)$, $(4,0)$ and $(6,0)$. For K-type transition, the modes are $(1,1)$, $(1,0)$, $(2,1)$, $(2,0)$ and $(2,2)$. Finally, for oblique transition, the interpolated modes are $(1,1)$, $(2,0)$, $(1,3)$, $(0,2)$ and $(0,4)$. Readers are referred to Joslin *et al.* (1993), Lozano-Durán *et al.* (2018) and Gonzalez *et al.* (2023) for the specification of inlet frequencies and amplitudes corresponding to the transition scenarios.

Grid convergence studies are conducted using three progressively refined meshes, designated Mesh 0, Mesh 1 and Mesh 2, with grid refinement focused on improving resolution within the transitional boundary layer region. The sponge forcing is applied over a streamwise extent that encompasses the linear growth, nonlinear interaction and early breakdown phases of each transition type, ensuring that the full physics are captured by the PSE solution.

For H-type transition (Figure 1), the PSE-sponge method accurately captures the skin-friction curve behavior across all three meshes. All results exhibit a slower transitional skin-friction rise compared to the DNS, but the location of transition is consistent and accurate. The Mesh 0 result exhibits an underprediction of the peak skin-friction value and turbulent stress level, but this is improved upon in the successive grids. The coarse Mesh 0 result of the PSE-sponge simulation for K-type transition is relatively worse than the H-type. There is an unphysical kink and oscillation in the skin-friction curve through the transition region, and the subsequent turbulent stress is underpredicted. This can be seen in Figures 2 and 3. Nevertheless, the K-type transition simulations demonstrate robust convergence in the skin friction upon grid refinement. Refining the grid from Mesh 0 to Mesh 1, we observe that the oscillation in the skin friction vanishes, though there is still the presence of a kink in the PSE-sponge curve at $Re_x = 3.0 \cdot 10^5$. The stress in the turbulent region is slightly overpredicted on Mesh 1. The Mesh 2 simulation for K-type transition demonstrates good agreement with the WRLES through most of the computational domain, with only a slight overprediction of the peak skin friction. For

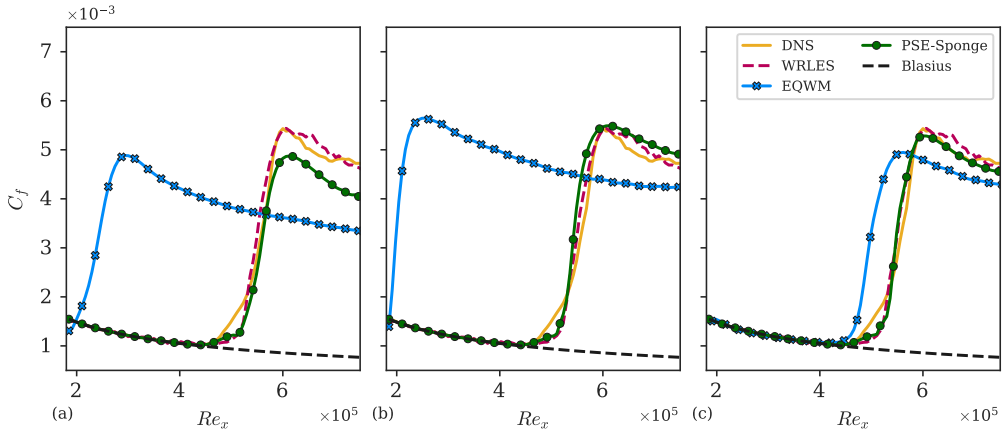


FIGURE 1. Skin-friction prediction for H-type transitional boundary layer using the PSE-sponge method on (a) Mesh 0, (b) Mesh 1 and (c) Mesh 2.

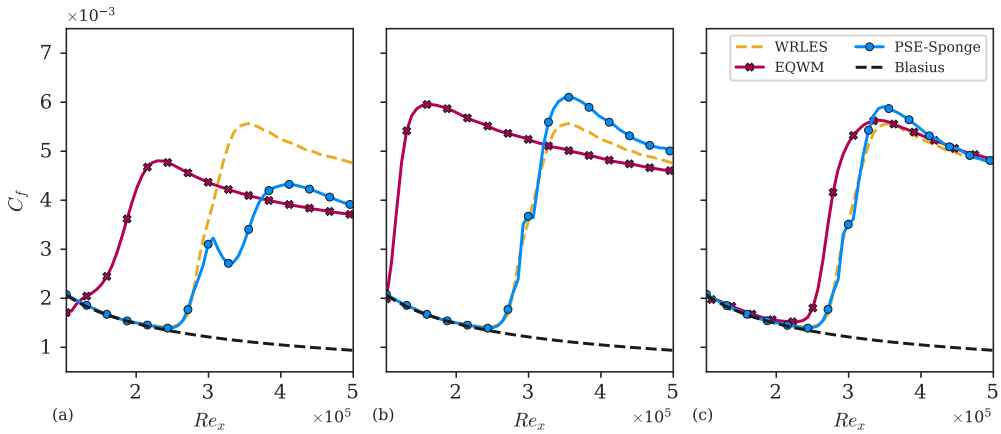


FIGURE 2. Skin-friction prediction for K-type transitional boundary layer using the PSE-sponge method on (a) Mesh 0, (b) Mesh 1 and (c) Mesh 2.

the oblique transition simulations, we observe poor agreement with the DNS reference solution due to the presence of an oscillation in the skin friction at $Re_x = 0.7 \cdot 10^6$ and an underprediction of the stress in the turbulent region of the flow. The results improve upon grid refinement. The location of transition is predicted accurately. The PSE-sponge simulations on Mesh 1 and 2 have a delayed skin friction rise compared to the DNS, which leads to the subsequent delayed location of the peak.

Instantaneous velocity contours from the coarsest mesh (Mesh 0) simulations are presented in Figures 4, 5 and 6. These visualizations confirm that the PSE-sponge method successfully reproduces the characteristic flow structures associated with each transition type. For H-type transition, the staggered Λ-vortex formation is clearly visible, and the oblique transition case shows the development of spanwise-periodic streaks and their eventual breakdown to turbulence. The K-type PSE-sponge velocity contours are blurred

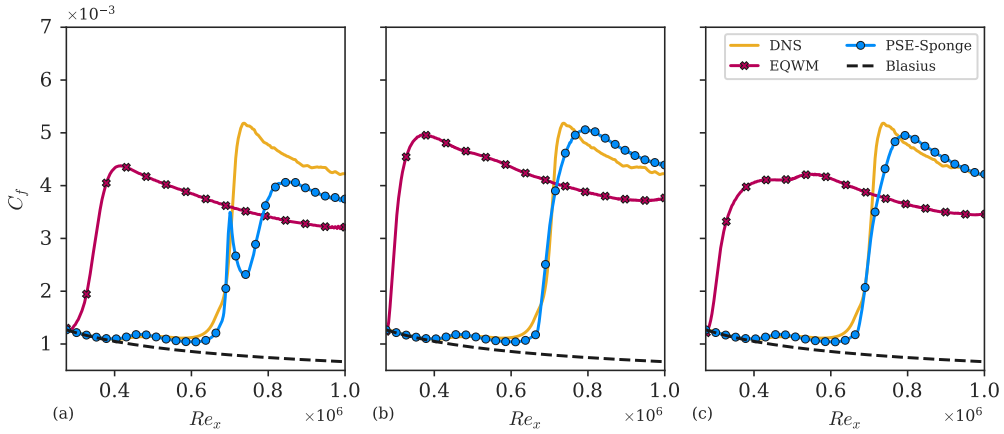


FIGURE 3. Skin-friction prediction for oblique transitional boundary layer using the PSE-sponge method on (a) Mesh 0, (b) Mesh 1 and (c) Mesh 2.

| Case | $\Delta x^+$ | $\Delta y^+$ | $\Delta z^+$ | $\frac{\lambda_x}{\Delta x}$ | $\frac{\delta_0}{\Delta y}$ | $\frac{\lambda_z}{\Delta z}$ | $N_x$ | $N_y$ | $N_z$ | $N_{cv}$ |
|---|---|---|---|---|---|---|---|---|---|---|
| Mesh 0 | 51.6 | 17.4 | 27.4 | 18.8 | 4 | 36.5 | 650 | 60 | 80 | 3.12E6 |
| Mesh 1 | 51.6 | 8.6 | 27.4 | 18.8 | 8 | 36.5 | 650 | 120 | 80 | 6.24E6 |
| Mesh 2 | 25.8 | 8.6 | 13.7 | 37.6 | 8 | 73.0 | 1300 | 120 | 160 | 2.50E7 |

TABLE 1. Mesh resolution in inner unit scaling for the three PSE-sponge H-type transition simulations. Inner units are scaled by the maximum $u_\tau$ in the domain. We also report the number of grid points contained within the 99% boundary-layer thickness at the inlet of the domain.

| Case | $\Delta x^+$ | $\Delta y^+$ | $\Delta z^+$ | $\frac{\lambda_x}{\Delta x}$ | $\frac{\delta_0}{\Delta y}$ | $\frac{\lambda_z}{\Delta z}$ | $N_x$ | $N_y$ | $N_z$ | $N_{cv}$ |
|---|---|---|---|---|---|---|---|---|---|---|
| Mesh 0 | 40.8 | 13.8 | 18.0 | 25.5 | 4 | 43.7 | 900 | 60 | 175 | 9.45E6 |
| Mesh 1 | 40.8 | 6.8 | 18.0 | 25.5 | 8 | 43.7 | 900 | 120 | 175 | 1.89E7 |
| Mesh 2 | 33.4 | 6.8 | 15.7 | 31.2 | 8 | 50.0 | 1100 | 120 | 200 | 2.64E7 |

TABLE 2. Mesh resolution in inner unit scaling for the three PSE-sponge K-type transition simulations. Inner units are scaled by the maximum $u_\tau$ in the domain. We also report the number of grid points contained within the 99% boundary-layer thickness at the inlet of the domain.

compared to the WRLES reference solution but nevertheless weakly exhibit the formation of the streamwise-aligned Λ-vortices.

Mesh resolutions for all grids used in the H-type, K-type and oblique transition simulations are shown in Tables 1 – 3. The results demonstrate that the PSE-sponge simulations require orders of magnitude fewer computational volumes for accurate results compared to DNS and WRLES.

The sensitivity of the PSE-sponge method to the sponge strength parameter $\sigma$ is examined through a parametric study focusing on H-type transition. Figure 7 demonstrates

| Case | $\Delta x^+$ | $\Delta y^+$ | $\Delta z^+$ | $\frac{\lambda_x}{\Delta x}$ | $\frac{\delta_0}{\Delta y}$ | $\frac{\lambda_z}{\Delta z}$ | $N_x$ | $N_y$ | $N_z$ | $N_{cv}$ |
|---|---|---|---|---|---|---|---|---|---|---|
| Mesh 0 | 51.7 | 18.0 | 32.8 | 27.5 | 4 | 44.0 | 800 | 70 | 88 | 4.93E6 |
| Mesh 1 | 51.7 | 8.9 | 32.8 | 27.5 | 8 | 44.0 | 800 | 140 | 88 | 9.86E6 |
| Mesh 2 | 41.3 | 8.9 | 23.1 | 34.4 | 8 | 62.5 | 1000 | 140 | 125 | 1.75E7 |

TABLE 3. Mesh resolution in inner unit scaling for the three PSE-sponge oblique transition simulations. Inner units are scaled by the maximum $u_\tau$ in the domain. We also report the number of grid points contained within the 99% boundary-layer thickness at the inlet of the domain.

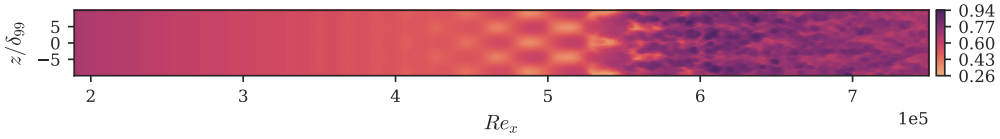


FIGURE 4. PSE-sponge instantaneous $u$ velocity contour plotted at $y^+ = 20$ for a zero-pressure gradient boundary layer (ZPGBL) undergoing H-type transition using Mesh 0.

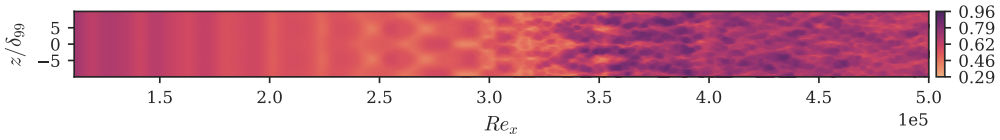


FIGURE 5. PSE-sponge instantaneous $u$ velocity contour plotted at $y^+ = 20$ for a ZPGBL undergoing K-type transition using Mesh 0.

that the method exhibits well-behaved convergence with respect to $\sigma$. For values below $\sigma = 0.5$, the sponge forcing becomes insufficient to effectively drive the LES solution toward the PSE target state, resulting in degraded prediction of transition location and skin-friction evolution. However, for $\sigma \geq 0.5$, the results achieve convergence, with minimal variation in the skin-friction profiles. This finding establishes a practical guideline for sponge parameter selection while demonstrating the method's robustness across a reasonable range of forcing strengths.

Similarly, the sensitivity to the number of PSE modes included in the sponge forcing is assessed in Figure 8. The difference in results between the simulations with three and five modes is negligible, but increasing the quantity of interpolated modes to eight shows a significant improvement in the prediction of skin friction. With eight interpolated modes, there is a much higher peak skin friction that is in line with the prediction from the WRLES. While some variation is observed with different mode counts, all configurations yield satisfactory results. One important consideration is the importance of mesh resolution when interpolating from the PSE grid to the WMLES grid. Higher harmonics have smaller spatial scales and faster timescales, which can therefore modify the time-step and resolution requirements.

### 3.2. *NLF(01)-0416 airfoil*

The NLF(01)-0416 airfoil represents a case of practical relevance to the aerospace industry due to its potential for drag reduction and fuel savings through extended laminar

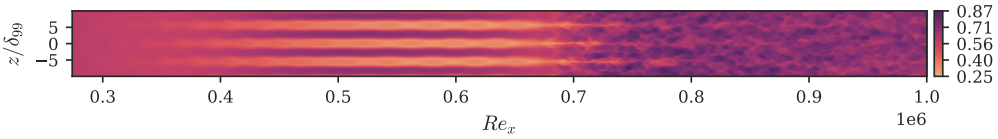


FIGURE 6. PSE-sponge instantaneous $u$ velocity contour plotted at $y^+ = 20$ for a ZPGBL undergoing oblique transition using Mesh 0.

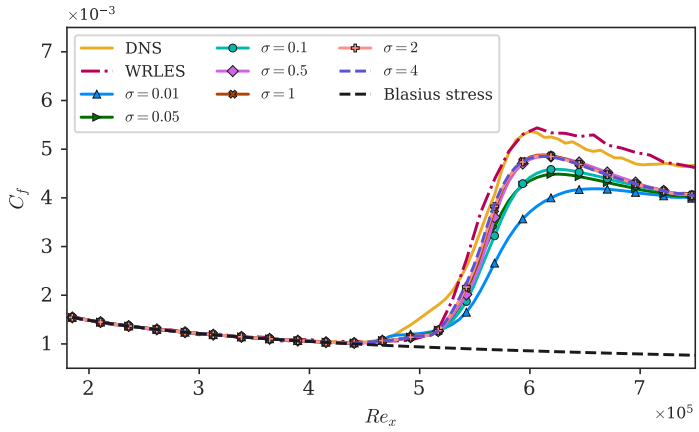


FIGURE 7. Skin friction versus $Re_x$ for the H-type transitional boundary layer, demonstrating sensitivity to the strength of the sponge parameter $\sigma$. Simulations are performed on Mesh 0 with 5 modes.

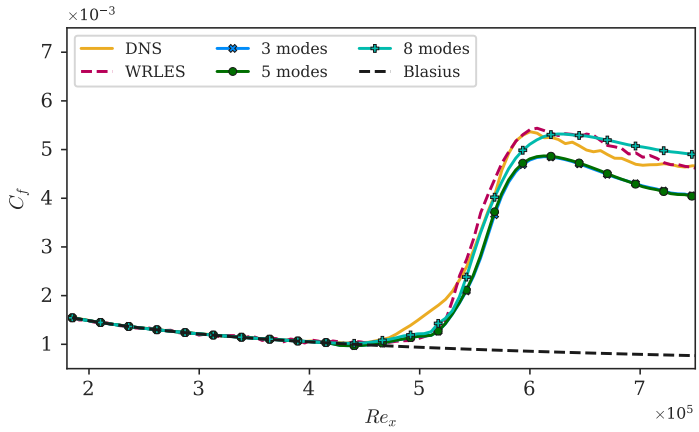


FIGURE 8. Skin friction versus $Re_x$ for the H-type transitional boundary layer demonstrating sensitivity to the number of modes present in the NLPSE simulation. Simulations are performed on Mesh 0 with $\sigma = 0.5$.

flow regions on both the upper and lower surfaces. Natural laminar flow airfoils are specifically designed to maintain laminar boundary layers over substantial portions of their chord length, thereby reducing skin-friction drag compared to conventional airfoils where transition occurs near the leading edge.

The experimental investigation of the NLF(01)-0416 airfoil conducted by Somers at NASA Langley's Low-Turbulence Pressure Tunnel provides a reference case for the validation of transitional-flow simulations (Somers 1981). For the present study, we focus on the $\alpha = 0°$, $Ma = 0.1$, $Re_c = 4 \times 10^6$ case, which exhibits natural transition that occurs on both the upper and lower surfaces of the airfoil. The experimental data provide surface pressure distributions and integrated force coefficients, though detailed skin-friction measurements are not available. However, calibrated RANS-based computational studies of this configuration exist in the literature, providing additional benchmarks for comparison of skin-friction evolution and transition location (Griffin *et al.* 2024).

The computational grid is a spherical domain constructed using Voronoi cells, with the far-field boundary positioned at 25 chord lengths from the airfoil surface. This domain size ensures that far-field boundary conditions do not influence the near-body flow physics while maintaining computational efficiency. Three levels of grid refinement are systematically tested to assess mesh convergence of the PSE-sponge methodology when applied to complex geometries.

Following the methodology established for flat-plate configurations, the simulation process begins with a precursor computation employing only the Falkner-Skan wall model as the boundary condition. This precursor simulation generates laminar boundary layer profiles along the airfoil surface without the complications introduced by transition modeling or subgrid-scale effects. The FSWM results demonstrate good agreement with Reynolds-averaged Navier-Stokes (RANS) predicted skin-friction distributions in the laminar portions of both the upper and lower surfaces, validating the approach for generating accurate baseflow states. The boundary-layer profiles extracted from the FSWM solution provide the initial conditions for subsequent NLPSE analysis, ensuring that the stability calculations are performed using physically consistent base flows.

A critical consideration in applying the PSE-sponge method to the NLF airfoil concerns the specification of initial disturbance characteristics. Unlike the flat-plate validations, where disturbance parameters were inherited from established literature, the airfoil configuration lacks a formal receptivity analysis to determine the natural disturbance environment. This limitation necessitates a calibration approach similar to that employed in $e^N$ transition prediction methods, where disturbance amplitudes are adjusted to achieve transition locations that match experimental observations. While this approach introduces some empiricism into the methodology, it represents a practical compromise that enables the simulation of realistic configurations. Future developments could focus on incorporating receptivity models to eliminate this calibration requirement and achieve fully predictive, physics-based transition prediction.

For the present simulations, H-type transition is specified on both the upper and lower surfaces of the airfoil, based on the understanding that this mechanism is prevalent in low-disturbance environments typical of natural laminar flow applications. The disturbance parameters are tailored for each surface to account for the different pressure gradient environments encountered. For the upper surface, the fundamental TS wave frequency is set to $F = \omega\nu/U_\infty = 40$ and the subharmonic spanwise wave number is $\beta = 0.02$, while the mode amplitudes are specified as $A_{TS} = 1 \times 10^{-5}$ and $A_{SH} = 1 \times 10^{-7}$. The lower surface is specified identically. The wall-normal extent of the PSE domain is set to 0.025 chord lengths for both surfaces, ensuring adequate coverage of the boundary-layer region while maintaining computational efficiency.

To establish the effectiveness of the PSE-sponge methodology for complex geometries and identify optimal parameter settings, a parametric study is conducted examining both

sponge strength sensitivity and grid-convergence behavior. The analysis compares PSE-sponge results against standard LES approaches using the equilibrium wall model and no-slip boundary conditions. This comparison framework enables assessment of the PSE-sponge method's performance relative to current standard practice while demonstrating its advantages for transitional-flow simulation. RANS skin-friction data from the literature serves as the benchmark solution. The sponge strength parameter $\sigma$ is varied across three values: 0.005, 0.05 and 0.5, representing weak, moderate and strong forcing levels, respectively. Each parameter setting is evaluated on three progressively refined meshes (Mesh 0, Mesh 1 and Mesh 2) to assess grid-convergence characteristics. Preferential refinement of the Voronoi cells near the walls of the airfoil is used in the grid-refinement study. Progressively refined grids decrease the finest characteristic size of the cells by a factor of two. The EQWM and CLES (coarse LES, i.e., with no-slip wall boundary conditions) simulations are computed on identical grids, providing direct comparison of the methods' mesh sensitivity and transition-prediction capabilities.

The $\sigma$ sensitivity analysis on Mesh 0 is presented in Figure 9, which demonstrates the critical importance of adequate sponge-forcing strength for accurate transition prediction. The weakest forcing levels ($\sigma = 0.005$ and $\sigma = 0.05$) both overpredict the skin-friction rise on both upper and lower surfaces, indicating insufficient coupling between the PSE solution and the LES field. The strongest forcing ($\sigma = 0.5$) also overpredicts the peak skin friction but to a lesser extent. All three of these simulations, however, do demonstrate the characteristics of a transitioning boundary layer on both sides of the airfoil. The upper side transition location is upstream of the RANS reference data, while the lower side transition location is accurate. This suggests that even on the coarsest mesh, adequate sponge strength can partially capture the transition process. All PSE-sponge simulations perform reasonably well in returning to the turbulent stress in the fully turbulent regions downstream of transition. In contrast, the EQWM simulation exhibits essentially turbulent skin-friction levels throughout the entire airfoil surface on both upper and lower surfaces, consistent with the premature transition behavior observed in the flat-plate studies. The EQWM mispredicts the skin friction everywhere except in regions where the flow is genuinely turbulent. The no-slip boundary condition simulation demonstrates the opposite failure mode, essentially never transitioning on either surface, again reflecting the behavior observed in previous flat-plate validations where insufficient grid resolution prevents the capture of transitional physics.

Grid-convergence behavior for the optimal sponge strength ($\sigma = 0.5$) is examined in Figure 10. The results demonstrate mesh convergence, with the finest grid (Mesh 2) providing the best agreement with RANS reference data (Griffin *et al.* 2024). All PSE-sponge simulations overpredict the skin-friction peak at the leading edge on both the upper and lower surfaces. This is due to the Falkner-Skan wall model. Possible remedies to improve the FSWM prediction of this flow are a Reynolds number correction (Dauricio & Azevedo 2023) and a curvature correction to the Falkner-Skan similarity solution (Ramirez & Araya 2022). On all grids and for both the upper and lower surfaces, the stress predictions from the PSE-sponge simulations quickly begin agreeing with the reference data after the leading edge. On the upper side of the airfoil, the rise in wall stress due to transition occurs slightly upstream of the reference data, and the magnitude of the overshoot is also overpredicted. As the grid is refined, the magnitude of the peak skin-friction overprediction decreases and approaches the reference data. Finally, there is satisfactory agreement for the turbulent stress. On the lower side of the airfoil, the transition location is more accurately predicted and shows favorable agreement with the

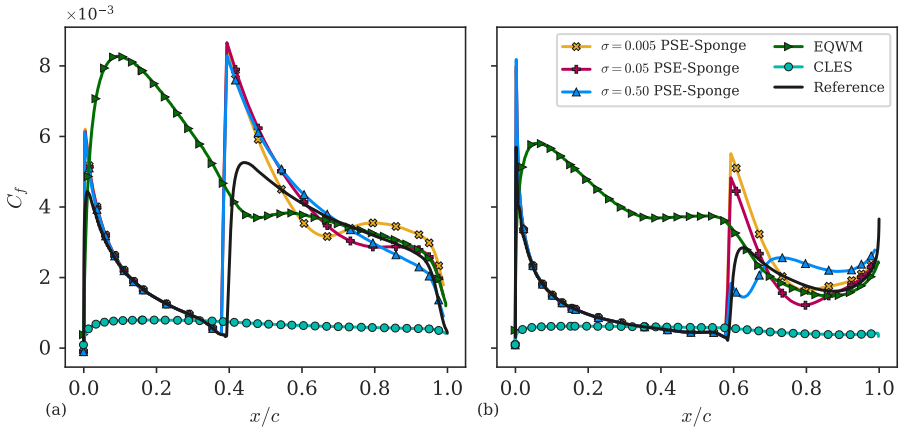


FIGURE 9. Skin-friction coefficient for Mesh 0 simulations on (a) the upper surface and (b) the lower surface using the PSE-sponge with varying strengths of $\sigma$, EQWM and CLES. Reference data from Griffin *et al.* (2024).

reference data. On the coarsest grid, there is an oscillation in the skin friction right after transition, a phenomenon that was also observed on the coarse grid PSE-Sponge simulations of K-type and oblique transition. Upon grid refinement, the oscillation in the stress vanishes and more reasonable results are obtained. On the finest grid simulated, there is still a slight overprediction of the turbulent stress.

The practical implications of these modeling differences are illustrated in the force coefficient evolution plot shown in Figure 11. The drag coefficient histories, plotted against nondimensional time $t/t_{FT}$, where $t_{FT}$ represents the flow transit time over one chord length, reveal the differences between approaches. The EQWM overpredicts the drag coefficient due to its premature transition and excessive skin friction. The CLES does accurately predict the drag coefficient; however, this is due to error cancellation in the skin friction. In the upstream portion of the flow prior to transition, CLES overpredicts the skin friction, while in the downstream portion of the flow after transition the friction is underpredicted. Overall, the CLES fails to predict the transitional behavior. The PSE-sponge method, despite some inaccuracies in the transition and skin-friction predictions, provides a substantially more accurate drag estimate, because it captures the transition location and extent more faithfully. When compared against experimental values and industry-standard CFD prediction tolerances (10 drag counts, where 1 drag count = 0.0001 $\Delta C_D$), the PSE-sponge results fall within acceptable engineering accuracy limits, while the traditional approaches exceed these tolerances (Levy *et al.* 2014). Similar trends are observed for lift coefficient prediction, though the sensitivity is less pronounced due to the predominantly pressure-driven nature of lift generation.

## 4. Conclusions

This study was inspired by Slotnick *et al.* (2014) which raised the issue that laminar and transitional flow were a computational bottleneck for the use of WMLES in computational fluid dynamics. Traditional equilibrium wall models, designed for fully turbulent flows, fail in transitional boundary layers, leading to premature transition and inaccurate predictions of skin friction and drag. To bridge the gap between computational efficiency

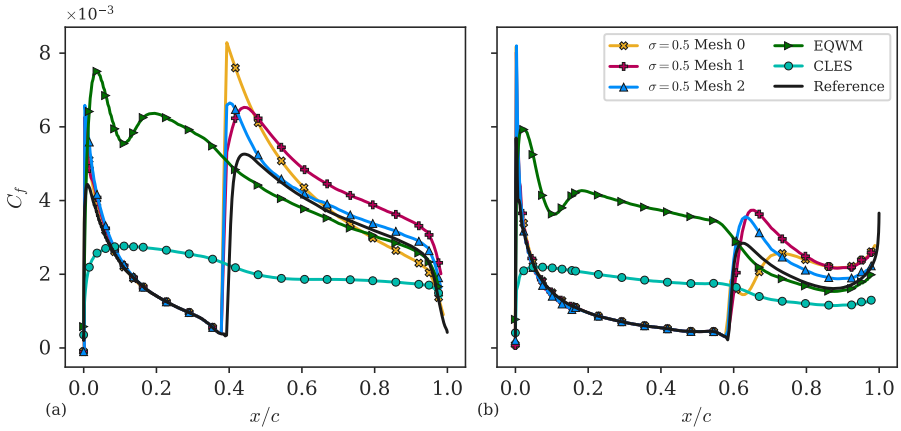


FIGURE 10. Skin-friction coefficient convergence for $\sigma = 0.5$ simulations using the PSE-sponge on (a) the upper surface and (b) the lower surface. EQWM and no-slip simulations are shown for Mesh 2. Reference data from Griffin *et al.* (2024).

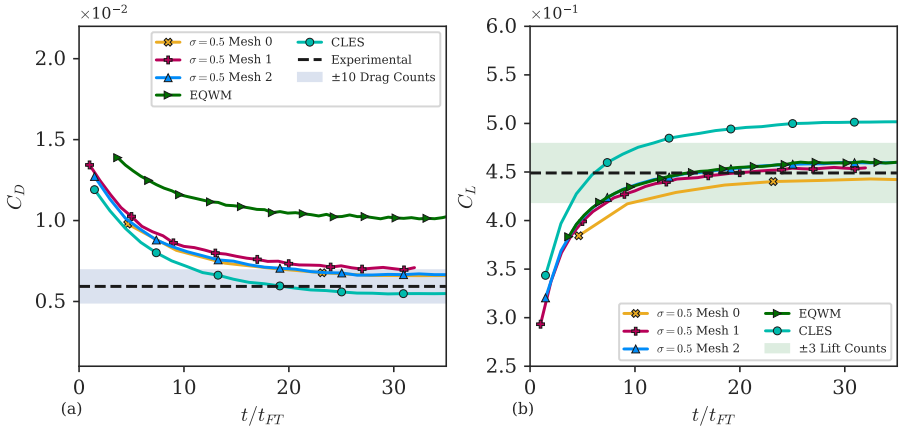


FIGURE 11. (a) Drag coefficient and (b) lift coefficient versus nondimensional time. Experimental data from Somers (1981).

and physical accuracy, we developed a unified framework combining nonlinear parabolized stability equations with WMLES. The framework employs a Falkner-Skan wall model that accurately captures laminar boundary layers without the 10–100 times grid refinement penalty of Navier-Stokes simulations, providing physically consistent base states for stability analysis. The PSE-sponge methodology was developed and implemented in the unstructured flow solver charLES (Bres *et al.* 2018; Goc *et al.* 2021) and was shown to leverage the computational efficiency of stability analysis while maintaining high-fidelity physics representation.

## Acknowledgements

This work was supported by the NASA Transformational Tools and Technologies Program (grant #80NSSC20M0201). This research used resources from the Oak Ridge Lead-

ership Computing Facility, which is a DOE Office of Science User Facility supported under Contract DE-AC05-00OR22725. The authors gratefully acknowledge helpful discussions with Professor Michael Karp, Professor Adrian Lozano-Duran, Dr. Kevin P. Griffin, and Dr. Sanjeeb Bose.

## REFERENCES

Berlin, S., Wiegel, M. & Henningson, D. S. 1999 Numerical and experimental investigations of oblique boundary layer transition. *J. Fluid Mech.* **393**, 23–57.

Bertolotti, F. P., Herbert, T. & Spalart, P. R. 1992 Linear and nonlinear stability of the Blasius boundary layer. *J. Fluid Mech.* **242**, 441–474.

Brés, G. A., Bose, S. T., Emory, M., Ham, F. E., Schmidt, O. T., Rigas, G. & Colonius, T. 2018 Large-eddy simulations of co-annular turbulent jet using a Voronoi-based mesh generation framework. In *2018 AIAA/CEAS Aeroacoustics Conference*, p. 3302. Reston, VA: AIAA.

Choi, H. & Moin, P. 2012 Grid-point requirements for large eddy simulation: Chapman's estimates revisited. *Phys. Fluids* **24**, 011702.

Dauricio, E. T. V. & Azevedo, J. L. F. 2023 A wall model for external laminar boundary layer flows applied to the wall-modeled LES framework. *J. Comput. Phys.* **484**, 112087.

Goc, K. A., Lehmkuhl, O., Park, G. I., Bose, S. T. & Moin, P. 2021 Large eddy simulation of aircraft at affordable cost: a milestone in computational fluid dynamics. *Flow* **1**, E14.

Gonzalez, C. A., Harris, S. R. & Moin, P. 2021 Falkner-skan wall model baseflow generation for the parabolized stability equations. *Annual Research Briefs*, Center for Turbulence Research, Stanford University, pp. 73–81.

Gonzalez, C. A., Harris, S. R. & Moin, P. 2023 Simulating an H-type transitional boundary layer in a coupled NLPSE and WMLES framework with a Falkner-Skan wall model. *Annual Research Briefs*, Center for Turbulence Research, Stanford University, pp. 307–320.

Gonzalez, C. A., Harris, S. R. & Moin, P. 2024 glimpse: an open-source incompressible nonlinear parabolized stability equation solver. *Annual Research Briefs*, Center for Turbulence Research, Stanford University, pp. 231–243.

Gonzalez, C. A., Karp, M. & Moin, P. 2020 Wall-stress modeling for laminar boundary layers in coarse grids. *Annual Research Briefs*, Center for Turbulence Research, Stanford University, pp. 85–95.

Griffin, K. P., Lee, B., Vijayakumar, G., Bornhoft, B., Shende, O. B. & Whitmore, M. P. 2024 Pressure-gradient-based RANS model for separation in transitional and turbulent flows. *Proceedings of the Summer Program*, Center for Turbulence Research, Stanford University, pp. 53-63.

Herbert, T. 1988 Secondary instability of boundary layers. *Annu. Rev. Fluid Mech.* **20**, 487–526.

Herbert, T. 1997 Parabolized stability equations. *Annu. Rev. Fluid Mech.* **29**, 245–283.

Joslin, R. D., Streett, C. L. & Chang, C.-L. 1993 Spatial direct numerical simulation of boundary-layer transition mechanisms: Validation of PSE theory. *Theor. Comput. Fluid Dyn.* **4** (6), 271–288.

Kachanov, Y. S., Kozlov, V. V. & Levchenko, V. Y. 1977 Nonlinear development of a wave in a boundary layer. *Fluid Dyn.* **12**, 383–390.

Klebanoff, P. S., Tidstrom, K. D. & Sargent, L. M. 1962 The three-dimensional nature of boundary-layer instability. *J. Fluid Mech.* **12**, 1–34.

Levy, D. W., Laflin, K. R., Tinoco, E. N., Vassberg, J. C., Mani, M., Rider, B., Rumsey, C. L., Wahls, R. A., Morrison, J. H., Brodersen, O. P. *et al.* 2014 Summary of data from the Fifth Computational Fluid Dynamics Drag Prediction Workshop. *J. Aircr.* **51**, 1194–1213.

Lozano-Durán, A., Hack, M. J. P. & Moin, P. 2018 Modeling boundary-layer transition in direct and large-eddy simulations using parabolized stability equations. *Phys. Rev. Fluids* **3**, 023901.

Ramirez, M. & Araya, G. 2022 Falkner-Skan similarity flow solutions subject to wall curvature and passive scalar transport. *TFEC-2022-40936.*

Slotnick, J. P., Khodadoust, A., Alonso, J., Darmofal, D., Gropp, W., Lurie, E. & Mavriplis, D. J. 2014 CFD vision 2030 study: a path to revolutionary computational aerosciences. *NF1676L-18332.*

Somers, D. M. 1981 Design and experimental results for a natural-laminar-flow airfoil for general aviation applications. *Tech. Rep. 1865, NASA.*